Title
The lithiation process and Li diffusion in amorphous SiO2 and Si from first-principles

Authors
Sivonxay, E
Aykol, M
Persson, KA

Publication Date
2020-01-20

DOI
10.1016/j.electacta.2019.135344

Peer reviewed

Electrochimica Acta 331 (2020) 135344

Contents lists available at ScienceDirect

Electrochimica Acta

journal homepage: www.elsevier.com/locate/electacta

The lithiation process and Li diffusion in amorphous SiO_2 and Si from first-principles

Eric Sivonxay [a, b], Muratahan Aykol [a, c], Kristin A. Persson [a, b, *]

[a] Energy Storage and Distributed Resources Division, Lawrence Berkeley National Laboratory, Berkeley, CA, 94720, United States
[b] Department of Materials Science, University of California Berkeley, Berkeley, CA, 94720, United States
[c] Toyota Research Institute, Los Altos, CA, 94022, United States

ARTICLE INFO

Article history:
Received 25 July 2019
Received in revised form
2 November 2019
Accepted 19 November 2019
Available online 25 November 2019

Keywords:
Li-Ion batteries
Alloy anodes
Silicon anode
Density functional theory calculations
Ab-initio molecular dynamics

ABSTRACT

Silicon is considered the next-generation, high-capacity anode for Li-ion energy storage applications, however, despite significant effort, there are still uncertainties regarding the bulk Si and surface SiO_2 structural and chemical evolution as it undergoes lithiation and amorphization. In this paper, we present first-principles calculations of the evolution of the amorphous Si anode, including its oxide surface layer, as a function of Li concentration. We benchmark our methodology by comparing the results for the Si bulk to existing experimental evidence of local structure evolution, ionic diffusivity as well as electrochemical activity. Recognizing the important role of the surface Si oxide (either native or artificially grown), we undertake the same calculations for amorphous SiO_2, analyzing its potential impact on the activity of Si anode materials. Derived voltage curves for the amorphous phases compare well to experimental results, highlighting that SiO_2 lithiates at approximately 0.7 V higher than Si in the low Li concentration regime, which provides an important electrochemical fingerprint. The combined evidence suggests that i) the inherent diffusivity of amorphous Si is high (in the order $10^{-9}cm^2s^{-1}$ - $10^{-7}cm^2s^{-1}$), ii) SiO_2 is thermodynamically driven to lithiate, such that Li—O local environments are increasingly favored as compared to Si—O bonding, iii) the ionic diffusivity of Li in Li_ySiO_2 is initially two orders of magnitude lower than that of Li_ySi at low Li concentrations but increases rapidly with increasing Li content and iv) the final lithiation product of SiO_2 is Li_2O and highly lithiated silicides. Hence, this work suggests that - excluding explicit interactions with the electrolyte - the SiO_2 surface layer presents a kinetic impediment for the lithiation of Si and a sink for Li inventory, resulting in non-reversible capacity loss through strong local Li—O bond formation.

1. Introduction

Due to their high theoretical gravimetric capacity, alloys have garnered much attention as potential high energy density anodes in energy storage applications [1—3]. Specifically, silicon exhibits a theoretical maximum gravimetric capacity of 3579mAh/g, an order of magnitude greater than that of the state-of-the-art graphite anode (~ 372mAh/g) [4]. While several other values for theoretical gravimetric capacity corresponding to formation of $Li_{21}Si_5$[5,6] (4008mAh/g) and $Li_{22}Si_5$[7—10] (4199mAh/g), it has been shown that these phases cannot be reversibly formed, even when cycling at elevated temperatures [4,5]. Silicon also suffers from several performance-inhibiting attributes stemming from its large volumetric expansion under lithiation and its chemical reactivity with the liquid electrolyte. The large volume expansion (up to 300%) of the Si electrode results in mechanical pulverization and loss of electrical contact which reduces the capacity as well as the cycle life of the system. Efforts to reduce the degradation have been creative ranging from i) the use of nano-sized particles/architectures [11—15], ii) thin films [16—18], to iii) porous or hollow particle [19—21], and iv) core-shell particles [22—24]. Common to all these attempts is the increased Si surface area to volume ratio, which, while alleviating the internal strain under lithiation, also increases the reactivity with the electrolyte, lowers the volumetric energy density of the composite anode and increases the amount of native surface SiO_2. The growth of SiO_2 on Si has been well studied both in the semiconductor and the energy storage field, and is found to be

* Corresponding author. Department of Materials Science, University of California Berkeley, Berkeley, CA, 94720, United States.
E-mail address: kapersson@lbl.gov (K.A. Persson).

https://doi.org/10.1016/j.electacta.2019.135344

tunable, in composition, thickness, and crystallinity, by varying the concentration of oxygen, water present and temperature during the synthesis process [25]. The native SiO_2 surface layer on bulk Si anode particles is usually found to be amorphous due to its rapid formation under ambient conditions, and strain with respect to the underlying Si phase[26]. However, despite recent attention, the native oxide layer's impact on the Si anode electrochemical performance remains elusive[27]. On one hand, the presence of SiO_2 has been suggested to promote a first-cycle functional surface electrolyte interface (SEI) formation through the passivation of the anode [28,29]. Core-shell architectures consisting of a SiO_z layer grown on a Si nanotube were, as a "mechanical clamping layer", found to restrict Si swelling to the interior channel [28]. Additional studies on sub-stoichiometric silicon oxides (SiO_z for $z < 2$) suggest the oxide layer is active during the cycling of the material. Jung et al. [30] used first-principles molecular dynamics to investigate the lithiation behavior of substoichiometric amorphous SiO, finding a theoretical capacity of 3172mAh/g corresponding to the composition $Li_{5.22}SiO$. Furthermore, they also hypothesized that a SiO anode, thermodynamically evolves towards Li–Si alloys and Li-silicates($Li_2Si_2O_5$, $Li_6Si_2O_7$, Li_4SiO_4)/Li_2O, respectively [30]. In a similar study, Chou et al. [31] used first principles to study the structural evolution of amorphous $SiO_{1/3}$ during lithiation, finding an increase in the Li–Si bonding and the formation of Li_6O complexes.

On the other hand, bulk SiO_2 exhibits a high impedance, caused by its low electrical conductivity and low Li mobility [32]. Hence, some studies suggest that, as opposed to bulk SiO_2 [33], a thin SiO_2 surface layer remains inert under lithiation, due to the activation energy and overpotential required to break the strong Si–O bonds. For example, Ariel et al. reported on the use of a 9 nm SiO_2 film as a solid electrolyte. By monitoring the voltage of the Li_yCoO_2/SiO_2/Si cells while charging, they suggested that SiO_2 was both electrically insulating and unreactive to Li, allowing for Li transport from the Li_yCoO_2 to the Si to form Li_ySi [33]. In contrast, other reports claim that SiO_2 surface films react with Li to form lithium silicates, Li silicides and even Li_2O upon lithiation [11,34–36]. Zhang et al. [34] studied the structural evolution, electronic conductivity, and ionic conductivity of Li in SiO_2 films on SiC nanowires. The lithiation of the SiO_2 thin film was observed by TEM, revealing the presence of Li_2O and Li_4SiO_4 upon lithiation of amorphous SiO_2. Multiple reports show that a thicker SiO_2 surface layer causes increased irreversible capacity loss and low coulombic efficiency, due to Li consumption in the first cycle [29,35].

Numerous experimental studies on the diffusivity of Li in c-Si and a-Si report highly disparate values ranging from $10^{-16}cm^2s^{-1}$ - $10^{-8}cm^2s^{-1}$ in Refs. Li_xSi [18,37–46]. Diffusivity of $10^{-9}cm^2s^{-1}$ to $10^{-7}cm^2s^{-1}$ is found in amorphous Li_ySi (for $0 < y < 3.75$) and $10^{-10}cm^2s^{-1}$ to $10^{-9}cm^2s^{-1}$ in c-Si using ab-initio molecular dynamics (AIMD) [47,48]. Using nudged-elastic band (NEB) and Kinetic Monte Carlo (KMC), the diffusivity of Li in c-Si is found to be $10^{-13}cm^2s^{-1}$ to $10^{-12}cm^2s^{-1}$ [49,50], even as low as $10^{-16}cm^2s^{-1}$ to $10^{-8}cm^2s^{-1}$ in a study by Yan et al. [51] Similar to the range of results and conclusions pertaining to the reactivity of SiO_2, the ionic conductivity and Li kinetics of amorphous SiO_2, as a function of lithium content is contentious. Li diffusion in Li_4SiO_4 was studied using 2-D NMR techniques, which yielded high relaxation times, correlating to high Li activation energies of 756–850 meV and 530–700 meV, for the crystalline [52] and polycrystalline [53] Li_4SiO_4 phases, respectively. In the amorphous phases, Gobel et al.[54] found conflicting activation energies within the same sample using NMR and electrical conductivity measurements; 228 meV and 673 meV. A recent study by Ostadhossein et al. also found slow Li diffusion using reactive force fields in amorphous Li_ySiO_2 for $0.5 < y < 3.5$ and suggested a concave diffusion behavior with concentration; $10^{-15}cm^2s^{-1}$ for $y = 0.5$, increasing to $10^{-9}cm^2s^{-1}$ at $y = 1.5$ and then decreasing again to $10^{-13}cm^2s^{-1}$ at $y = 2.5$ [55]. The opposite trend is observed by Zhang et al. using AIMD, finding monotonic decreasing diffusivity for $0.1 < y < 1.0$ in amorphous Li_ySiO_2 [34]. On the other hand, Du et al. [56] reported consistently high diffusivities of $10^{-4}cm^2s^{-1}$ - $10^{-5}cm^2s^{-1}$ in glassy $yLi_2O-(1-y)SiO_2$ at 800K using classical molecular dynamics simulations. Additionally, Jung et al. [30] find a high Li diffusivity of $1.8 \times 10^{-8}cm\ s^{-2}$ in crystalline Li_2O using NEB.

The widely varying results for Li diffusion in silicon oxides motivate a revisit, in particular using a consistent methodology, comparing transport in amorphous Si with SiO_2. Previous work has focused on crystalline systems, such as $Li_2Si_2O_5$, $Li_6Si_2O_7$, Li_4SiO_4, and Li_2O [30], and amorphous Si and Li_ySi [47–51], with only one study of Li_ySiO_2 for $0.1 < y < 1$ [34]. In particular, the Li insertion kinetics and structural evolution of Li_ySiO_2 has only been studied, using first principles calculations, within a subset of the lithiation range, $0 < y_{Li} < 1$, despite a maximum theoretical lithiation capacity of $0 < y_{Li} < 8.2$. In this paper we investigate the lithiation thermodynamics and kinetics of amorphous Li_ySiO_2 for the full concentration range $0 < y_{Li} < 8.2$, using Density Functional Theory (DFT) and AIMD and compare its properties - using the same methodology - to the crystalline phases as well as to bulk amorphous and crystalline Si.

2. Computational methods

2.1. Density Functional Theory calculations

The Vienna Ab-Initio Simulation Package (VASP)[57,58] was used for all first-principles calculations presented. We use the projector augmented-wave (PAW) potentials[59] along with the Perdew-Burke-Ernzerhof (PBE) generalized-gradient functional (GGA) [60]. In structure optimization calculations, all lattice parameters and atomic positions were fully relaxed using a plane wave cutoff of 520 eV, at a minimum reciprocal lattice *k*-point density of 64 per $Å^3$. The parameters used for all calculations are extensively benchmarked by the Materials Project and can be found in the Python Materials Genomics (pymatgen) documentation in the MP Relax and MP Static sets [61]. Structures for the crystalline materials were taken from the Materials Project whereas amorphous structures are created as described in section 2.2. Ab-initio molecular dynamics (AIMD) simulations were performed with the NVT ensemble as implemented in VASP using a time-step of 2 fs, with a plane wave cutoff of 400 eV and one gamma centered k-point to reduce the computational cost.

2.2. Generating amorphous structures

An AIMD based workflow was used to generate representative amorphous structures for Li_ySi and Li_ySiO_2, for $0 < y < 5$ according to a 'melt-quench' methodology previously demonstrated on several amorphous oxide systems [62,63]. The workflows for generating amorphous structures are constructed using the pymatgen, Fireworks, and atomate software packages[61,64,65], and are available at http://github.com/materialsproject/mpmorph. First, atoms were randomly distributed in a cubic simulation cell following the desired composition using packmol[66], at a density $\sim$ 20% larger than the crystalline compounds. Unit cell sizes were constrained to $\sim$ 100 atoms to ensure reasonable runtime of AIMD simulations. Thus, we note that for some of the high Li content structures, few Si atoms are present. The pressure was then

equilibrated through a series of constant temperature AIMD simulations at 3000 K, rescaling the unit cell between each AIMD simulation until an internal pressure of 0 bar was realized, and a stable melt is obtained. Energy equilibration was achieved in a 10 ps simulation before snapshots of the melt were collected at regular intervals from a final 10 ps production run. The snapshots of the system were quenched following a stepped cooling scheme with 400 fs cooling and 1 ps isothermal steps. Final structures were optimized using VASP with higher precision parameters compatible with the Materials Project calculations, as described above in section 2.1.

2.3. Lithiation thermodynamics

The formation energy (U_F) for the amorphous phases is calculated with respect to crystalline termini (Si, Li, and O_2) as;

$$U_F(\mathrm{Li_ySiO_z}) = U_{\mathrm{Li_ySiO_z}} - yU_{Li} - \frac{z}{2}U_{O_2} - U_{Si} \quad (1)$$

where $U_{Li_ySiO_z}$, U_{Li} and U_{Si} represent the DFT-calculated ground state energies of the silicides/silicates, bcc Li and diamond cubic Si, respectively, in units of eV/atom. U_{O_2} is the energy per atom (eV/atom) of O_2 with an applied gas correction [67]. The ground state energies are used to construct the low-temperature phase diagram, and the electrode potential (E) of each phase triangle is obtained as:

$$\mu_{Li} - \mu_{Li}^0 = neE \quad (2)$$

where μ_{Li} is the chemical potential of Li in a lithiated phase, μ_{Li}^0 is the reference chemical potential of bcc Li metal, e is the elementary charge of an electron, and n is the number of Li inserted. Under this framework, the calculated electrode potentials are referenced to the Li/Li^+ reference electrode, and will be provided as such throughout this article. The chemical potentials of μ_{Li}, μ_{Si}, and μ_O in each phase region are calculated by solving a set of linear equations, one per each stable phase, as in eq. (3) [68].

$$G_{rxn}^i = \sum_{j=Li,Si,O_2} x_j^i \mu_j \quad (3)$$

Here, x represents the mole fraction of element j within phase i. At room temperature, ΔG can be approximated by the change in ground state energy, $\Delta G_{rxn} \approx \Delta U_{rxn}$ [69,70]. For the lithiation of Si, $\Delta U_{rxn} = U_F(\mathrm{Li_ySi})$, while the in the lithiation of SiO_2, $\Delta U_{rxn} = U_F(\mathrm{Li_ySiO_z}) - U_F(\mathrm{SiO_z})$.

The gravimetric capacity, C (mAh/g), of each Li_ySi or Li_ySiO_2 phase is calculated according to the following equation.

$$C = \frac{yN_Ae}{MW} * 4.45 * 10^{-20} \quad (4)$$

where N_A is Avogadro's number, MW is the molecular weight of the starting electrode, 28.09 $gmol^{-1}$ and 60.08 $gmol^{-1}$ for Li_ySi and Li_ySiO_2, respectively, and $4.45*10^{-20}$ is the conversion factor from the elementary charge, e, to mAh.

2.4. Lithium diffusion

Following the simulation of amorphous structures discussed in section 2.2, the Li diffusivity was calculated from AIMD simulations at 500 K, 1000 K, and 1500 K. Three starting structures, equally spaced, were chosen from the 3000 K AIMD trajectories, the volume of the cell was equilibrated for each temperature (P = 0 kbar) before production runs. From the trajectories, the mean square displacement (MSD) as a function of time t is calculated with time-averaging to improve the collected statistics as:

$$\langle \mathbf{r}^2(t) \rangle \approx \frac{1}{N(T-t)} \sum_{i=1}^{N} \int_0^{T-t} [\mathbf{r}_i(t'+t) - \mathbf{r}_i(t')]^2 dt' \quad (5)$$

here $\mathbf{r}$ is the vector of unwrapped coordinates of each atom, N is the number of diffusing atoms, T is the total simulation time, t' is the lag time, and i is the Li atom index. The diffusion coefficient, D, is obtained from the slope of the MSD versus time in the linear regime. We used 200 ps AIMD simulations and an upper bound of 70% of the maximum simulation time in determining D [71]. The diffusion coefficient at room temperature, 25 °C, is obtained through extrapolation of an Arrhenius model fitted to the average D values calculated for each of the three high-temperature AIMD simulations. Estimated numerical errors of the diffusion coefficient are obtained from the variance-covariance matrix, for the regression to the Arrhenius equation, through the propagation of uncertainty.

3. Results and discussion

In the following sections we present and discuss the resulting Si and SiO_2 amorphous structures and their short-range order motifs and benchmark the structures against previous experimental results, as well as the phase stability, voltage profiles, and Li diffusion as a function of Li content.

3.1. Short range order and Si connectivity in amorphous Li_ySi and Li_ySiO_2

First, we establish that the resulting 'melt-quench' Li_ySi amorphous phases are good representatives of the local structures formed during electrochemical Li intercalation, e.g. by comparing them to the short-range order motifs previously established experimentally [72,73]. To probe the medium-range order of the system, the Si networks were examined over the composition range using a clustering approach that identifies groups of Si atoms based on bonding and connectivity. Two Si are said to belong to the same aggregate if there is a path between them passing through other bonded Si atoms [74]. The clustering summarized in Fig. 1 qualitatively agrees with previous reports[73] on Li_ySi local motifs. As a function of increasing Li content, we observe that a Si network structure is initially present before y = 0.5 (LiSi), as shown in the

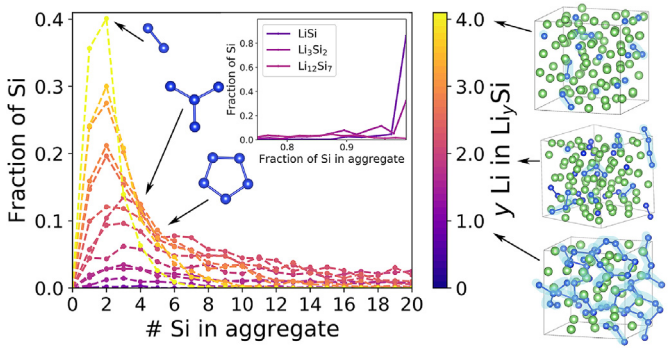

Fig. 1. Aggregation of Si in Li_ySi for $0 < y < 4.2$, where the x-axis indicates the size of the Si group and y-axis shows the fraction of Si in each group size. Color indicates composition, as seen on the color scale. Inset shows the aggregation of Si in networked regime, with x-axis indicating fraction of Si in the simulation cell that compose the aggregate. Representative structural motifs are highlighted to the right, with Si atoms show in blue and Li atoms in green. (For interpretation of the references to color in this figure legend, the reader is referred to the Web version of this article.)

inset of Fig. 1, rapidly breaking up into smaller clusters by y = 1.7 ($Li_{12}Si_7$). Thereafter, a gradual transition occurs between y = 1.7 and y = 3.25 ($Li_{13}Si_4$) where the Si aggregates no longer percolate through the structure, leading to an increasing amount of Si dumbbells and isolated Si. The formation of small clusters previously described[72,73,75] appear at y = 1.7. At compositions y > 3.25, dumbbells dominate although a sizeable fraction of 4-atom clusters exhibiting linear as well 'Y' (see Fig. 1) arrangements, similar to those seen in crystalline $Li_{12}Si_7$ [76], are also present. In the highest lithiated state studied, y = 4.2, isolated Si and dumbbells are the most prevalent motifs. While the breakup of the Si network and formation of clusters would be expected for random atomic configurations, with decreasing Si concentration, the formation of these Si aggregates is not commensurate of truly homogeneously distributed atoms, suggesting that the structures formed capture the chemical interactions between the Li and Si atoms. This is supported by charge population studies conducted by Chevrier et al. [77,78] and Kim et al.[79] of amorphous and crystalline Li_ySi, which show a significant increase in Si charge state and nearly constant charge state for Li with increasing Li content, suggesting Si charge state is dependent, primarily, on its local environment. An equivalence of Si charge state in the amorphous and crystalline phase is also observed, further confirming the similarity of the Si local environment in both the amorphous and crystalline states. Hence, in summary, we believe that an acceptable agreement between the simulated amorphous Li_ySi local motifs and those found by electrochemical lithiation is established.

In order to understand the evolution of local arrangement and ionic coordination in the computationally-derived amorphous SiO_2, as a function of lithiation, we follow a similar procedure. The simulated amorphous SiO_2 structure exhibits sharp peaks corresponding to Si–Si, Si–O, and O–O bonding centered at 0.30 nm, 0.18 nm, and 0.28 nm respectively. As a comparison, the average bond lengths in the amorphous lithium silicides for Si–Si, Si–Li, and Li–Li are found at 0.24 nm, 0.26 nm, and 0.27 nm, respectively. With increased Li content in SiO_2, a new peak appears in the Si–Si bonding at 0.24 nm as seen in Fig. 2a, characteristic of the Si–Si bond length in Si and Li_ySi. This peak grows with the addition of Li, indicative of the formation of more Si–Si bonds, until y = 3 where the peak's decline is seen due to the formation of isolated Si atoms, characteristic to $Li_{21}Si_5$. As more Li is added, this peak grows in magnitude until the initial 0.30 nm bonding disappears by y = 3, indicating a break up of the Si–Si network. In parallel, the O–O peak (see Fig. 2b) at 0.31 nm, corresponding to Li_2O bond lengths, increases in height which indicates formation of Li_2O environments. Hence, the overall trend with lithiation of amorphous SiO_2 is increasing Li–O and Li–Si bond formation, at the expense of Si–O bonding, in agreement with previous results on substoichiometric SiO_z [31,80]

To further examine the short-range order and network formation in the silicates,the analysis applied to the lithium silicides Li_ySi is modified to extract coordination and connectivity information for the multiple species found in the Li–Si–O system. Here, Si and/or O are defined to exist in the same aggregate if a path links the two through bonded Si and/or O atoms. Within this approach, the aggregates belong to one of three groups (indicated in Fig. 3 by color); i) those containing Si and O, ii) those with only Si, and iii) the O which only binds to Li e.g. Li_2O environments. Similar to the Si-networks in the silicides, the silicates are found to maintain large Si–O networks in amorphous SiO_2 and $LiSiO_2$ as seen in Fig. 3. Lithiation past $LiSiO_2$ causes network fragmentation and isolation of substoichiometric SiO_z regions. Beyond z = 1, Fig. 3b–d), the formation of Li_2O environments are also observed. Consequently, a decrease of the O/Si ratio in Li–Si–O clusters, for aggregate sizes < 0.2, between Fig. 3c and d is observed, commensurate of the formation of Li_2O -like environments at the expense of Li_ySiO_z. Comparisons between the observed local environments and the prediction of thermodynamically stable phases are elaborated upon in Sec. 3.2.

3.2. The lithiation process in the Li–Si–O system

Fig. 4a) shows the calculated Li–Si–O phase diagram at low temperature, which is constructed from the calculated formation energies (for details, see section 2.3), for the crystalline and amorphous phases respectively. The convex hull, which constructs the energy envelope of the thermodynamically stable phases[81], is depicted with lines and the low-temperature stable phases as nodes along those lines. We emphasize that metastable compounds, e.g. those with energies above the convex hull, may be observed experimentally if the energy difference is small compared to the room temperature driving force for structural reorganization, similar to the case of amorphous Si.

Fig. 4b) shows the binary convex hull for the Li–Si composition line in the phase diagram, where the calculated crystalline and amorphous metastable phases are indicated. We note that $Li_{15}Si_4$ and $Li_{22}Si_5$ are both experimentally observed silicides[82–84], exhibiting formation energies of 1 meV/atom (within the accuracy of the employed DFT methodology) and 18 meV/atom above the hull, respectively. Similarly, we note that the amorphous states exhibit a high degree of metastability, ranging from 10 to 500 meV/atom, above the convex hull, however, the convex hull for the amorphous phases alone follow a similar trend as for their crystalline counterparts, as a function of Li content, in agreement with Kim et al. [79] This suggests that the *relative* difference in formation energy between compositions originates primarily from changes in short-range order Li–Si motifs. We note the importance of adapting the local structure to the chemical evolution, as simply replacing Si

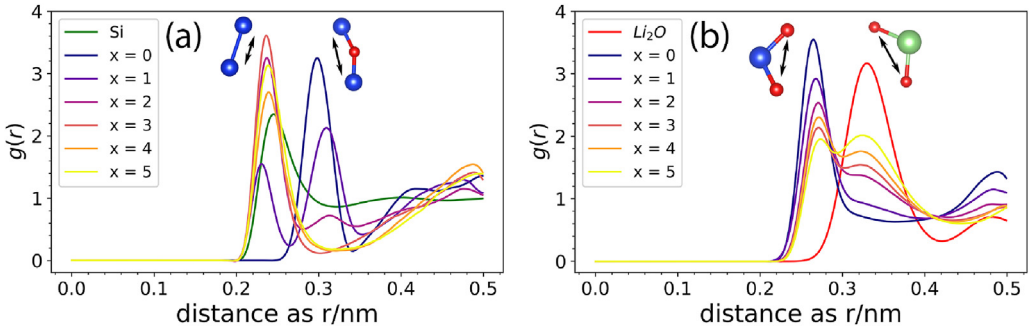

Fig. 2. Radial distribution functions of a) Si–Si and b) O–O pairs in amorphous. Li_ySiO_2

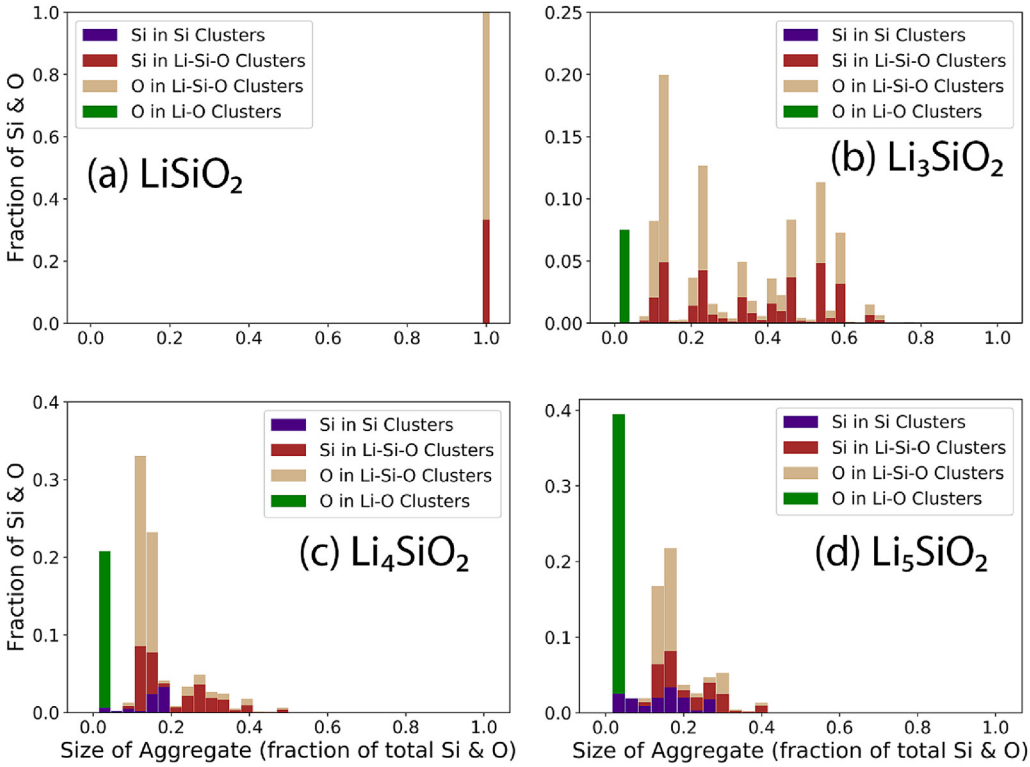

Fig. 3. a-d) Cluster size distributions in amorphous Li_ySiO_2 for y = 1, 3, 4, & 5. Similar to Fig. 1, the x-axis indicates the fraction of the Si & O in the structure in each cluster and the y-axis shows the fraction of Si and/or O within that cluster. Colored bars represent the Si or O in the 3 types of aggregates, as specified in the text.

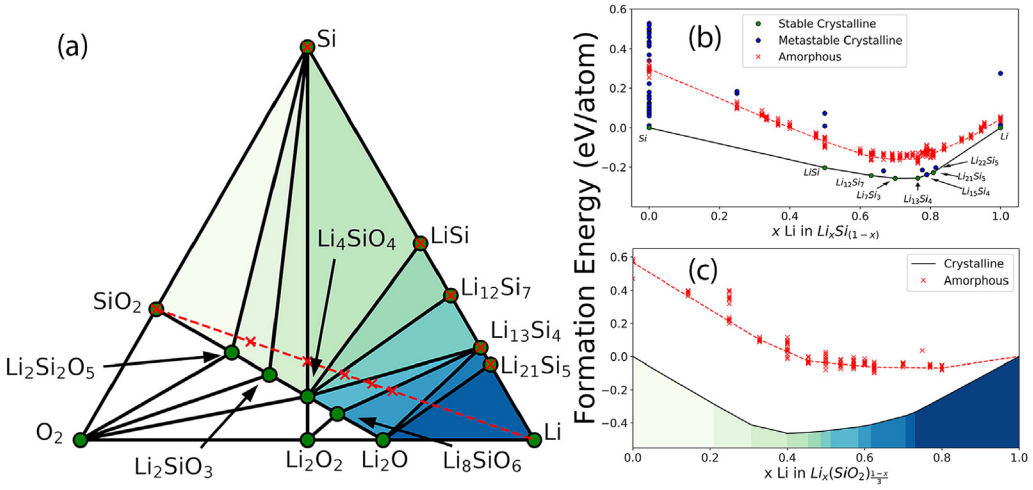

Fig. 4. a) Si–Li–O phase diagram, including calculated amorphous states and crystalline phases from the Materials Project, shown as red X's and green circles, respectively. Also shown is the formation energies of the crystalline as well as amorphous b) Li silicides with respect to crystalline Si and Li and c) Li silicates with respect to crystalline SiO_2 and Li. (For interpretation of the references to color in this figure legend, the reader is referred to the Web version of this article.)

with Li on an fcc lattice is thermodynamically unfavorable [50,85]. The formation energies, in Fig. 4b), exhibit a minimum around $x = 0.75$ corresponding to the composition with the largest reaction enthalpy, with respect to the terminal phases (e.g. $yLi + Si \rightarrow Li_ySi$). Amorphization of Si upon lithiation has previously been reported as an electrochemically-driven solid-state process[86,87], where regions of high Li concentration contribute electrons to the anti-bonding sp^3 orbitals of Si, weakening the Si–Si bonds allowing the formation of metastable amorphous phases. We further note that the high degree of metastablility of the amorphous phases suggests that crystallization is limited by kinetics. Crystallization of the $Li_{15}Si_4$ phase, however, has been observed in experimental studies [75,88] and rationalized as the interplay of higher diffusivity and the lack of Si–Si bonds in the structure. The formation energy plots in Fig. 4 b) provide additional insight into the crystallization. After Li_xSi_{1-x} amorphization, further lithiation will trace the amorphous curve in Fig. 4 b), however when the driving force for lithiation reaches 0, near $x_{Li} = 0.78 (3554 mAh/g)$, further Li incorporation into the amorphous matrix is no longer energetically favorable. Hence, alloying with additional Li occurs only through a

transformation from the amorphous to the crystalline phase, thus forming the $Li_{15}Si_4$ phase, which is the highest lithiated phase observed in experiments[73]. After c-$Li_{15}Si_4$ is formed, the formation of c- $Li_{21}Si_5$ is thermodynamically favorable, however, its absence in room temperature experiments suggests that the formation of $Li_{21}Si_5$ is kinetically hindered. This is in agreement with Kwon et al. who observe $Li_{21}Si_5$ only when lithiating between 100 and 120°C[5].

As indicated by the dashed line in Fig. 4a), SiO_2 is thermodynamically driven to lithiate. The predicted lithiation process passes through ten 3-phase regions consisting of lithium silicides, silicon, and stoichiometric lithium silicates, until the end products Li_2O and $Li_{21}Si_5$ are formed. Following this compositional trajectory, we examine the calculated formation energies of a range of Li_ySiO_2 amorphous compositions, shown in Fig. 4c), and compare to the combined energy of the crystalline phases as obtained through the convex hull of the phase diagram (illustrated by the same color scheme in Fig. 4a). Similar to the lithiation of Si, the amorphous structures are metastable as compared to the crystalline states and the overall shape of the lithiation convex hull is similar for both crystalline and amorphous phases. Again, the common trend suggests that the energy differences between the compositions are dominated by the local Li–Si–O environments, rather than longer range interactions, which are dissimilar in the crystalline and amorphous states. In the initial charging (lithiation of the anode), Si will be locally extruded within the native oxide layer, thereby forming lithium silicate environments. As shown in Fig. 4a), the formation of lithium silicates will occur for any composition of non-stoichiometric SiO_z, for $z < 2$, that may be found on the Si. Further charging will promote various Li silicide formation until Li_2O, $Li_{13}Si_4$, and $Li_{21}Si_5$ are formed. This agrees well with the analysis of local structural environments in amorphous Li_ySiO_z reported in Sec. 3.1 which predicts formation of short-range Li_2O domains past $Li_{2.9}SiO_2$. Although lithium silicides are predicted to form for $y > 2$, based on the phase diagram, pure Li–Si environments are scarce in the amorphous Li_ySiO_2 structures observed until $y = 4$ (Li_4SiO_2). We believe this may in part be due to artificial limitations in simulation unit cell size (see Section 2.2) and as such, not necessarily representative of real samples. Both clustering analysis as well as phase diagram thermodynamics indicate that Si-only clusters are common to amorphous Li_4SiO_2 and Li_5SiO_2 (Fig. 3c–d)) compositions as well as amorphous $Li_{13}Si_4$ (Fig. 1). Both compositions lie within the phase triangle formed by the Li_4SiO_4, Li_2O, and $Li_{13}Si_4$, hence the Si dumbbells, Si_4 chains, Y shapes, and Si_5 rings present in $Li_{13}Si_4$ are expected. The silicides are distributed in clusters of size 1–6 evidenced by (relatively) large peaks around sizes 4 and 5 in Li_4SiO_2 and 1, 2, and 4 in Li_5SiO_2. We note that the composition Li_4SiO_4 forms a particularly stable node in the phase diagram, being present in 5 of the 10 phase triangles and having the lowest formation enthalpy, as seen in Fig. 4c). Indeed, Zhang et al. [34] observed the strong presence of both Li_2O and Li_4SiO_4 in lithiated SiO_2 - coated SiC nanowires. Similarly, Guo et al. [35] observed the presence of crystalline Li_4SiO_4 and Li_2O after the first cycle.

3.3. Voltage profile in amorphous Li_ySi and Li_ySiO_2

The equilibrium potential profiles of the systems were derived from the convex hull and phase diagram (section 3.2) as described in section 2.3 [69]. Within the Materials Project, several stable crystalline lithium silicide phases exist; LiSi, $Li_{12}Si_7$, $Li_{13}Si_4$, and $Li_{21}Si_5$. Other crystalline Li_ySi phases have been experimentally observed, e.g. Refs. $Li_{22}Si_5$ [82–84] which is found to be weakly metastable using the current computational methodology. In the calculated voltage profile for Li_ySi, Fig. 5a), the crystalline states follow a stepwise curve from 0.39V to 0V. On the other hand, the lithiation potential of the amorphous lithium silicides is initially found to be higher than the crystalline counterparts, 0.50 V until $C = 954 mAh/g$, where it drops below and smoothly follows the crystalline states. This is a similar trend to that found by Chevrier et al. with the exception that their initial lithiation potential is 0.43 V, a disparity, likely, arising from the difference in the method of obtaining the amorphous structures [77].

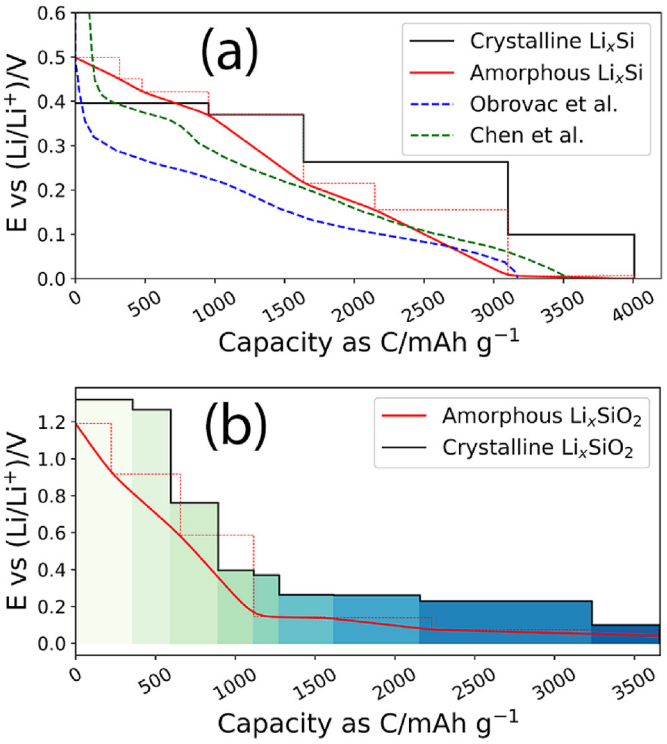

Fig. 5. Calculated electrode potential profile (E vs $(Li/Li^+)/V$) for crystalline and amorphous a) lithium silicides in comparison with experimental curves [18,89] and b) lithium silicates. The dashed red line in both a) and b) corresponds to the voltage of the amorphous phases as calculated from the convex hull before smoothing. (For interpretation of the references to color in this figure legend, the reader is referred to the Web version of this article.)

Similar to the case of Si lithiation, the potential profile for Li_ySiO_2, shown in Fig. 5b) was derived from the chemical potential of Li within the composition range between adjacent stable compositions. In the crystalline phases, the initial voltage of SiO_2 exceeds that of Si by almost 1 V. As lithiation progresses and a Li–Si environment forms, the voltage drops to values closer to that of Li_ySi. The amorphous phases follow a similar trajectory, initially exhibiting a potential of 1.2 V, and ending at 0.06 V. These findings agree qualitatively with experimental studies on bulk SiO_2 which exhibit voltage profiles higher than that of Si, between 1.0 and 1.5V [29,90,91]. The preferred equilibrium phase sequence upon lithiation shows the strength of, and preference towards, the formation of Li–Si and Li–O bonds at the expense of Si–O bonds. The formation of $Li_{13}Si_4$, $Li_{21}Si_5$, and Li_2O local environments is favored, even in the first charge, if the anode voltage drops below ≈ 100 mV vs Li/Li^+. During discharge, the lithiated composite (surface phase and bulk) will delithiate in order of increasing potential such that the lithium silicides within the oxide layer and silicides in the bulk Si will delithiate first, forming Li_ySi and Li_4SiO_4. Only after the Li_ySi phases have been completely delithiated will the Li_4SiO_4 be delithiated to form SiO_2. However, in practice, limits placed on cycling

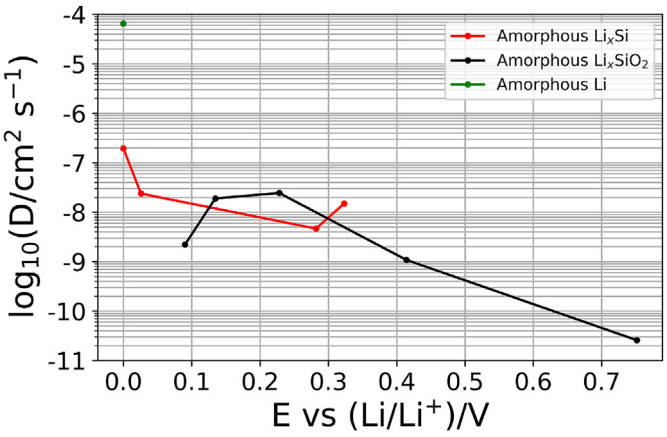

Fig. 6. Room temperature Li self-diffusion coefficients in amorphous lithium silicides and lithium silicates as a function of electrode potential E vs $(Li/Li^+)/V$.

window (e.g. 3 and 4.2V in $LiCoO_2$ based batteries[92]) may result in loss of energy density if the delithiation potential of the silicates is not reached, rendering the lithiation of the silicates functionally irreversible. This is in agreement with experimentally observed capacity losses, from the formation of inactive/irreversible Li_ySiO_z during the cycling of Li_ySiO_z [93], SiO[94], and SiO_z [29,95]. It is important to note that we do not explore the SiO_2/Si interface in this study and the aforementioned conclusion is drawn from the voltage profile of the bulk silicides and silicates.

3.4. *Li diffusion in amorphous Li_ySi and Li_ySiO_2*

Calculated Li diffusivities are shown in Fig. 6 and tabulated with corresponding errors in Table 1. Previous experimental reports of lithium diffusivity in amorphous Si vary between $10^{-16}cm^2s^{-1}$ - $10^{-7}cm^2s^{-1}$ [37,38]. We find self-diffusivity values near this range for all of the amorphous lithium silicides, with a general upward trend of diffusivity with increased Li insertion (decreasing voltage), in agreement with studies by Johari et al. and Wang et al. who find diffusivity increasing to $10^{-6}cm^2s^{-1}$ in $Li_{15}Si_4$ from $10^{-9}cm^2s^{-1}$ in Si, by studying the inter-diffusion of separate Li and Si layers using AIMD at high temperature. Intuitively, as percolating Li-rich environments and pathways are formed within the amorphous matrix (cluster analysis in Sec. 3.1), we expect the Li diffusivity in Li-rich Si to approach that of amorphous Li-metal. Literature values for Li self-diffusivity in Li metal range widely from $10^{-10}cm^2s^{-1}$ to $10^{-6}cm^2s^{-1}$ [96–98], presumably for polycrystalline samples. In the amorphous silicates, the Li self-diffusivity follows a different trend with composition. For $1 \leq y \leq 2$ ($LiSiO_2$ to Li_2SiO_2) it increases by 2 orders of magnitude. Visual inspection of the Li trajectories in $LiSiO_2$ shows expected high Li residence time near O and, with large plateaus within the MSD, for each individual Li atom, followed by Li hops to neighboring Si or O, indicating strong attraction between Li–O and Li–Si which increases the barrier for Li movement. However, once sub-stoichiometric SiO_z and Si environments are formed, the Li barrier to migration is lowered as Li moves through increasingly Li-rich environments. At $y = 3.0$, we expect silicide domains corresponding to an average composition of $Li_{12}Si_7$, which exhibits a similar Li diffusivity to that found in the composite lithium silicate matrix. This confirms that the formation of these local, yet connected domains, enable faster Li diffusion. As discussed previously, the Li_4SiO_2 and Li_5SiO_2 compositions share similar clustering patterns to $Li_{13}Si_4$ which gives rise to similar Li diffusion behavior. Overall, the trend shows that the presence of SiO_2 is likely to have a detrimental effect on overall rate behavior of a Si-based anode, especially at low levels of surface oxide lithiation. Irreversible formation of Li_2O environments will present a sink for Li inventory while formation of Si and lithium silicide environments will result in a higher Li diffusivity in subsequent cycles.

Table 1
Calculated Li self-diffusion coefficients in lithium silicides and silicates. Reported errors are statistical errors from the non-linear fit to the Arrhenius equation.

	E vs $(Li/Li^+)/V$	Diffusivity (D/cm^2s^{-1})	Fit Error (cm^2s^{-1})
LiSi	0.32	1.49E-08	6.35E-08
$Li_{12}Si_7$	0.28	4.65E-09	1.31E-08
$Li_{13}Si_4$	0.03	2.38E-08	2.44E-08
$Li_{21}Si_5$	0	1.96E-07	2.87E-07
$LiSiO_2$	0.75	2.58E-11	5.30E-14
Li_2SiO_2	0.41	1.08E-09	3.54E-10
Li_3SiO_2	0.23	2.44E-08	3.28E-09
Li_4SiO_2	0.13	1.90E-08	5.99E-10
Li_5SiO_2	0.09	2.21E-09	2.31E-10

4. Summary

We present first-principles calculations of amorphous Li_ySi and Li_ySiO_z, and evaluate their structural evolution, electrochemical voltage, and Li diffusion properties, as a function of Li concentration. The local environments in Li_ySi compare well with existing experimental results from electrochemical lithiation. Similar Si short-range motifs are formed in the amorphous lithium silicides as in the crystalline phases, showcasing the preference for formation of 5-membered rings, Y-shapes, and Si dumbbells. Thermodynamic lithiation potentials show that amorphous SiO_2 lithiates at a higher potential than Si, initially approximately 1.2 V vs Li metal. The structural evolution of the amorphous lithium silicates corroborates the thermodynamic lithiation pathway as evidenced in the phase diagram, showing strong preference towards the formation of Li–O and Si–Si bonds. Aggregation of Si in the amorphous lithium silicates also correlates well with the aggregation of the silicides within the same phase triangle. Initial electrochemical activity of SiO_2 is found at 1.3 V, as compared to $\sim$ 0.4 V in Si. Diffusivities of Li in the amorphous silicides are found to be high (order $10^{-9}cm^2s^{-1}$ - $10^{-7}cm^2s^{-1}$), increasing with composition, while the amorphous silicates start low ($\sim$ $10^{-11}cm^2s^{-1}$), increasing to $10^{-8}cm^2s^{-1}$. Formation of percolating Li networks at higher Li concentrations coincide with higher Li transport in both the silicides and silicates. In conclusion, we find that SiO_2 is thermodynamically driven to lithiate, by extrusion of Si and increased formation of Li–O bonds. SiO_2 also exhibits two orders of magnitude lower Li diffusivity at low Li concentration. Hence, excluding explicit interaction with the liquid electrolyte, we find that the SiO_2 surface may impede Li transport at low Li contents and contribute to loss of Li inventory through the formation of Li_2O during prolonged cycling.

Acknowledgement

This work was supported by the Battery Materials Research (BMR) program directed by Tien Duong and the Silicon Electrolyte Interface Stabilization (SEISta) Consortium directed by Brian Cunningham and managed by Anthony Burrell, under the Assistant Secretary for Energy Efficiency and Renewable Energy (EERE), Office of Vehicle Technologies of the U.S. Department of Energy Contract No. DE-AC0205CH11231. M. Aykol was supported as part of the Computational Materials Sciences Program funded by the U.S. Department of Energy, Office of Science, Basic Energy Sciences,

Materials Sciences and Engineering Division, award no. DE-SC0014607. This research used resources of the National Energy Research Scientific Computing Center, a DOE Office of Science User Facility supported by the Office of Science of the U.S. Department of Energy under contract no. DE-AC02-05CH11231. We also thank Nongnuch Artrith for fruitful discussions.

References

[1] J. Chen, Recent progress in advanced materials for lithium ion batteries, Materials 6 (2013) 156–183.
[2] C.-M. Park, J.-H. Kim, H. Kim, H.-J. Sohn, Li-alloy based anode materials for Li secondary batteries, Chem. Soc. Rev. 39 (2010) 3115.
[3] N. Nitta, G. Yushin, High-capacity anode materials for lithium-ion batteries: Choice of elements and structures for active particles, Part. Syst. Charact. 31 (2014) 317–336.
[4] M.N. Obrovac, L. Christensen, Structural changes in silicon anodes during lithium insertion/extraction, Electrochem. Solid State Lett. 7 (2004) A93–A96.
[5] J.Y. Kwon, J.H. Ryu, S.M. Oh, Performance of electrochemically generated Li21Si5 phase for lithium-ion batteries, Electrochim. Acta 55 (2010) 8051–8055.
[6] M.N. Obrovac, V.L. Chevrier, Alloy negative electrodes for Li-ion batteries, Chem. Rev. 114 (2014) 11444–11502.
[7] G.A. Tritsaris, K. Zhao, O.U. Okeke, E. Kaxiras, Di Ff Usion of Lithium in Bulk Amorphous Silicon : A Theoretical Study, 2012.
[8] T.L. Chan, J.R. Chelikowsky, Controlling diffusion of lithium in silicon nanostructures, Nano Lett. 10 (2010) 821–825.
[9] A. Casimir, H. Zhang, O. Ogoke, J.C. Amine, J. Lu, G. Wu, Silicon-based anodes for lithium-ion batteries: effectiveness of materials synthesis and electrode preparation, Nano Energy 27 (2016) 359–376.
[10] D. Thomas, M. Abdel-Hafiez, T. Gruber, R. Hüttl, J. Seidel, A.U. Wolter, B. Büchner, J. Kortus, F. Mertens, The heat capacity and entropy of lithium silicides over the temperature range from (2 to 873)K, J. Chem. Thermodyn. 64 (2013) 205–225.
[11] W.-S. Chang, C.-M. Park, J.-H. Kim, Y.-U. Kim, G. Jeong, H.-J. Sohn, Quartz (SiO2): a new energy storage anode material for Li-ion batteries, Energy Environ. Sci. 5 (2012) 6895.
[12] M. Wu, J.E. Sabisch, X. Song, A.M. Minor, V.S. Battaglia, G. Liu, In situ formed Si nanoparticle network with micron-sized Si particles for lithium-ion battery anodes, Nano Lett. 13 (2013) 5397–5402.
[13] L. Hu, H. Wu, S.S. Hong, L. Cui, J.R. McDonough, S. Bohy, Y. Cui, Si nanoparticle-decorated Si nanowire networks for Li-ion battery anodes, Chem. Commun. 47 (2011) 367–369.
[14] C. Chan, H. Peng, G. Liu, K. Mcllwrath, X. Zhang, R. Huggins, Y. Cui, High-performance lithium battery anodes using silicon nanowires, Nat. Nanotechnol. 3 (2007) 31–35.
[15] H. Li, X. Huang, L. Chen, G. Zhou, Z. Zhang, D. Yu, Y. Jun Mo, N. Pei, Crystal structural evolution of nano-Si anode caused by lithium insertion and extraction at room temperature, Solid State Ion. 135 (2000) 181–191.
[16] H. Jung, M. Park, Y.G. Yoon, G.B. Kim, S.K. Joo, Amorphous silicon anode for lithium-ion rechargeable batteries, J. Power Sources 115 (2003) 346–351.
[17] K.L. Lee, J.Y. Jung, S.W. Lee, H.S. Moon, J.W. Park, Electrochemical characteristics of a-Si thin film anode for Li-ion rechargeable batteries, J. Power Sources 129 (2004) 270–274.
[18] L.B. Chen, J.Y. Xie, H.C. Yu, T.H. Wang, An amorphous Si thin film anode with high capacity and long cycling life for lithium ion batteries, J. Appl. Electrochem. 39 (2009) 1157–1162.
[19] Y. Yao, M.T. McDowell, I. Ryu, H. Wu, N. Liu, L. Hu, W.D. Nix, Y. Cui, Interconnected silicon hollow nanospheres for lithium-ion battery anodes with long cycle life, Nano Lett. 11 (2011) 2949–2954.
[20] L. Lin, X. Xu, C. Chu, M.K. Majeed, J. Yang, Mesoporous amorphous silicon: a simple synthesis of a high-rate and long-life anode material for lithium-ion batteries, Angew. Chem. Int. Ed. 55 (2016) 14063–14066.
[21] X. Li, P. Meduri, X. Chen, W. Qi, M.H. Engelhard, W. Xu, F. Ding, J. Xiao, W. Wang, C. Wang, J.-G. Zhang, J. Liu, Hollow core–shell structured porous Si–C nanocomposites for Li-ion battery anodes, J. Mater. Chem. 22 (2012) 11014.
[22] L.-f. Cui, R. Ruffo, C.K. Chan, H. Peng, Y. Cui, Crystalline-Amorphous Core - Shell Silicon Nanowires for High Capacity and High Current Battery Electrodes 2009, 2009.
[23] N. Liu, H. Wu, M.T. McDowell, Y. Yao, C. Wang, Y. Cui, A yolk-shell design for stabilized and scalable Li-ion battery alloy anodes, Nano Lett. 12 (2012) 3315–3321.
[24] H. Kim, J. Cho, Superior lithium electroactive mesoporous Si @ carbon core - shell nanowires for lithium battery anode material, Nano Lett. 8 (2008) 3688–3691.
[25] B.E. Deal, A.S. Grove, General relationship for the thermal oxidation of silicon, J. Appl. Phys. 36 (1965) 3770–3778.
[26] N.V. Rumak, V.V. Khatko, Structure and properties of silicon dioxide thermal films (II), Phys. Status Solidi A 477 (1984) 477–484.
[27] M. Morita, T. Ohmi, E. Hasegawa, M. Kawakami, M. Ohwada, Growth of native oxide on a silicon surface, J. Appl. Phys. 68 (1990) 1272–1281.
[28] H. Wu, G. Chan, J.W. Choi, I. Ryu, Y. Yao, M.T. McDowell, S.W. Lee, A. Jackson, Y. Yang, L. Hu, Y. Cui, Stable cycling of double-walled silicon nanotube battery anodes through solid–electrolyte interphase control, Nat. Nanotechnol. 7 (2012) 310–315.
[29] J. Zhao, H.-W. Lee, J. Sun, K. Yan, Y. Liu, W. Liu, Z. Lu, D. Lin, G. Zhou, Y. Cui, Metallurgically lithiated SiOx anode with high capacity and ambient air compatibility, Proc. Natl. Acad. Sci. 113 (2016) 7408–7413.
[30] S.C. Jung, H.J. Kim, J.H. Kim, Y.K. Han, Atomic-Level understanding toward a high-capacity and high-power silicon oxide (SiO) material, J. Phys. Chem. C 120 (2016) 886–892.
[31] C.Y. Chou, G.S. Hwang, Lithiation behavior of silicon-rich oxide (SiO1/3): a first-principles study, Chem. Mater. 25 (2013) 3435–3440.
[32] S. Xun, X. Song, L. Wang, M.E. Grass, Z. Liu, V.S. Battaglia, G. Liu, The effects of native oxide surface layer on the electrochemical performance of Si nanoparticle-based electrodes, J. Electrochem. Soc. 158 (2011) A1260.
[33] N. Ariel, G. Ceder, D.R. Sadoway, E.A. Fitzgerald, Electrochemically controlled transport of lithium through ultrathin SiO2, J. Appl. Phys. 98 (2005).
[34] Y. Zhang, Y. Li, Z. Wang, K. Zhao, Lithiation of SiO2 in Li-ion batteries: in situ transmission electron microscopy experiments and theoretical studies, Nano Lett. 14 (2014) 7161–7170.
[35] B. Guo, J. Shu, Z. Wang, H. Yang, L. Shi, Y. Liu, L. Chen, Electrochemical reduction of nano-SiO2 in hard carbon as anode material for lithium ion batteries, Electrochem. Commun. 10 (2008) 1876–1878.
[36] N. Yan, F. Wang, H. Zhong, Y. Li, Y. Wang, L. Hu, Q. Chen, Hollow porous SiO2 nanocubes towards high-performance anodes for lithium-ion batteries, Sci. Rep. 3 (2013) 1568.
[37] E. Hüger, L. Dörrer, J. Rahn, T. Panzner, J. Stahn, G. Lilienkamp, H. Schmidt, Lithium transport through nanosized amorphous silicon layers, Nano Lett. 13 (2013) 1237–1244.
[38] T.L. Kulova, Y.V. Pleskov, A.M. Skundin, E.I. Terukov, O.I. Kon'kov, Lithium intercalation into amorphous-silicon thin films: an electrochemical-impedance study, Russ. J. Electrochem. 42 (2006) 708–714.
[39] A. Dunst, M. Sternad, V. Epp, M. Wilkening, Fast Li+Self-Diffusion in amorphous Li-Si electrochemically prepared from semiconductor grade, monocrystalline silicon: insights from spin-locking nuclear magnetic relaxometry, J. Phys. Chem. C 119 (2015) 12183–12192.
[40] C.S. Fuller, J.A. Ditzenberger, Diffusion of lithium into germanium and silicon [1], Phys. Rev. 91 (1953) 193.
[41] K. Yoshimura, J. Suzuki, K. Sekine, T. Takamura, Measurement of the diffusion rate of Li in silicon by the use of bipolar cells, J. Power Sources 174 (2007) 653–657.
[42] K.S.T.T.K. Yoshimura, J. Suzuki, Determination of the diffusion coefficient of lithium in, Silicon 441 (2005) 2017.
[43] M. Wu, B. Xu, C. Ouyang, Physics of electron and lithium-ion transport in electrode materials for Li-ion batteries, Chin. Phys. B 25 (2015).
[44] N. Ding, J. Xu, Y.X. Yao, G. Wegner, X. Fang, C.H. Chen, I. Lieberwirth, Determination of the diffusion coefficient of lithium ions in nano-Si, Solid State Ion. 180 (2009) 222–225.
[45] E.M. Pell, Diffusion rate of Li in Si at low temperatures, Phys. Rev. 119 (1960) 1222–1225.
[46] E. Hüger, L. Dörrer, H. Schmidt, Permeation, solubility, diffusion and segregation of lithium in amorphous silicon layers, Chem. Mater. 30 (10) (2018) 3254–3264, acs.chemmater.8b00186.
[47] P. Johari, Y. Qi, V.B. Shenoy, The mixing mechanism during lithiation of Si negative electrode in Li-ion batteries: an Ab initio molecular dynamics study, Nano Lett. 11 (2011) 5494–5500.
[48] Z. Wang, Q. Su, H. Deng, Y. Fu, Composition dependence of lithium diffusion in lithium silicide: a density functional theory study, ChemElectroChem 2 (2015) 1292–1297.
[49] G.A. Tritsaris, K. Zhao, O.U. Okeke, E. Kaxiras, Diffusion of lithium in bulk amorphous silicon: a theoretical study, J. Phys. Chem. C 116 (2012) 22212–22216.
[50] J. Moon, B. Lee, M. Cho, K. Cho, Ab initio and kinetic Monte Carlo simulation study of lithiation in crystalline and amorphous silicon, J. Power Sources 272 (2014) 1010–1017.
[51] X. Yan, A. Gouissem, P. Sharma, Atomistic insights into Li-ion diffusion in amorphous silicon, Mech. Mater. 91 (2015) 306–312.
[52] Z. Xu, J.F. Stebbins, Cation dynamics and diffusion in lithium orthosilicate : two-dimensional lithium-6 NMR A, Science 270 (1995) 1332–1334.
[53] M. Wilkening, P. Heitjans, Extremely slow cation exchange processes in Li4SiO4 probed directly by two-time 7Li stimulated-echo nuclear magnetic resonance spectroscopy, J. Phys. Condens. Matter 18 (2006) 9849–9862.
[54] E. Göbel, W. Müller-Warmuth, H. Olyschläger, H. Dutz, 7Li NMR spectra, nuclear relaxation, and lithium ion motion in alkali silicate, borate, and phosphate glasses, J. Magn. Reson. 36 (1969) 371–387, 1979.
[55] A. Ostadhossein, S.-Y. Kim, E.D. Cubuk, Y. Qi, A.C.T. van Duin, Atomic insight into the lithium storage and diffusion mechanism of SiO2/Al2O3 electrodes of lithium ion batteries: ReaxFF reactive force field modeling, J. Phys. Chem. A 120 (2016) 2114–2127.
[56] J. Du, C.H. Chen, Structure and lithium ion diffusion in lithium silicate glasses and at their interfaces with lithium lanthanum titanate crystals, J. Non-Cryst. Solids 358 (2012) 3531–3538.
[57] G. Kresse, J. Furthmüller, Efficiency of ab-initio total energy calculations for metals and semiconductors using a plane-wave basis set, Comput. Mater. Sci. 6 (1996a) 15–50.

[58] G. Kresse, J. Furthmüller, Efficient iterative schemes for ab initio total-energy calculations using a plane-wave basis set, Phys. Rev. B Condens. Matter Mater. Phys. 54 (1996b) 11169–11186.
[59] P.E. Blöchl, Projector augmented-wave method, Phys. Rev. B 50 (1994) 17953–17979.
[60] J.P. Perdew, K. Burke, M. Ernzerhof, Generalized gradient approximation made simple, Phys. Rev. Lett. 77 (1996) 3865–3868.
[61] S.P. Ong, W.D. Richards, A. Jain, G. Hautier, M. Kocher, S. Cholia, D. Gunter, V.L. Chevrier, K.A. Persson, G. Ceder, Python Materials Genomics (pymatgen): a robust, open-source python library for materials analysis, Comput. Mater. Sci. 68 (2013) 314–319.
[62] M. Aykol, K.A. Persson, Oxidation protection with amorphous surface oxides: thermodynamic insights from ab initio simulations on aluminum, ACS Appl. Mater. Interfaces 10 (2018) 3039–3045.
[63] M. Aykol, S.S. Dwaraknath, W. Sun, K.A. Persson, Thermodynamic limit for synthesis of metastable inorganic materials, Sci. Adv. 4 (2018), eaaq0148.
[64] A. Jain, S.P. Ong, W. Chen, B. Medasani, X. Qu, M. Kocher, M. Brafman, G. Petretto, G.-M. Rignanese, G. Hautier, D. Gunter, K.A. Persson, FireWorks: a dynamic workflow system designed for high-throughput applications, Concurrency Comput. Pract. Ex. 27 (2015) 5037–5059.
[65] K. Mathew, J.H. Montoya, A. Faghaninia, S. Dwarakanath, M. Aykol, H. Tang, I.-H. Chu, T. Smidt, B. Bocklund, M. Horton, J. Dagdelen, B. Wood, Z.-K. Liu, J. Neaton, S.P. Ong, K. Persson, A. Jain, Atomate, A high-level interface to generate, execute, and analyze computational materials science workflows, Comput. Mater. Sci. 139 (2017) 140–152.
[66] L. Martinez, R. Andrade, E.G. Birgin, J.M. Martinez, PACKMOL: a package for building initial configurations for molecular dynamics simulations, J. Comput. Chem. 30 (2009) 2158–2159.
[67] L. Wang, T. Maxisch, G. Ceder, Oxidation energies of transition metal oxides within the GGA+U framework, Phys. Rev. B Condens. Matter Mater. Phys. 73 (2006) 1–6.
[68] Y. Wang, Y. Zhang, C. Wolverton, First-principles studies of phase stability and crystal structures in Li-Zn mixed-metal borohydrides, Phys. Rev. B Condens. Matter Mater. Phys. 88 (2013) 1–10.
[69] M.K. Aydinol, A.F. Kohan, G. Ceder, K. Cho, J. Joannopoulos, Ab initio study of lithium intercalation in metal oxides and metal dichalcogenides, Phys. Rev. B 56 (1997) 1354–1365.
[70] A. Urban, D.-H. Seo, G. Ceder, Computational understanding of Li-ion batteries, npj Comput. Mater. 2 (2016) 16002.
[71] X. He, Y. Zhu, A. Epstein, Y. Mo, Statistical variances of diffusional properties from ab initio molecular dynamics simulations, npj Comput. Mater. 4 (2018).
[72] T.K.J. Koster, E. Salager, A.J. Morris, B. Key, V. Seznec, M. Morcrette, C.J. Pickard, C.P. Grey, Resolving the different silicon clusters in Li 12Si 7 by 29Si and 6,7Li solid-state NMR spectroscopy, Angew. Chem. Int. Ed. 50 (2011) 12591–12594.
[73] B. Key, R. Bhattacharyya, M. Morcrette, V. Seznec, J.M. Tarascon, C.P. Grey, Real-time NMR investigations of structural changes in silicon electrodes for lithium-ion batteries, J. Am. Chem. Soc. 131 (2009) 9239–9249.
[74] H.-H. Chiang, J.-M. Lu, C.-L. Kuo, First-principles study of the structural and dynamic properties of the liquid and amorphous Li–Si alloys, J. Chem. Phys. 144 (2016), 034502.
[75] K. Ogata, E. Salager, C.J. Kerr, A.E. Fraser, C. Ducati, A.J. Morris, S. Hofmann, C.P. Grey, Revealing lithium-silicide phase transformations in nano-structured silicon-based lithium ion batteries via in situ NMR spectroscopy, Nat. Commun. 5 (2014) 3217.
[76] R. Nesper, H.G. von Schnering, J. Curda, Li12Si7, eine Verbindung mit trigonal-planaren Si4-Clustern und isometrischen Si5-Ringen, Chem. Ber. 119 (1986) 3576–3590.
[77] V.L. Chevrier, J.R. Dahn, First principles studies of disordered lithiated silicon, J. Electrochem. Soc. 157 (2010) 392–398.
[78] V.L. Chevrier, J.W. Zwanziger, J.R. Dahn, First principles study of Li-Si crystalline phases: charge transfer, electronic structure, and lattice vibrations, J. Alloy. Comp. 496 (2010) 25–36.
[79] H. Kim, C.Y. Chou, J.G. Ekerdt, G.S. Hwang, Structure and properties of Li-Si alloys: a first-principles study, J. Phys. Chem. C 115 (2011) 2514–2521.
[80] H. Jung, B.C. Yeo, K.-R. Lee, S.S. Han, Atomistics of the lithiation of oxidized silicon (SiOx) nanowires in reactive molecular dynamics simulations, Phys. Chem. Chem. Phys. 18 (2016) 32078–32086.
[81] S.P. Ong, L. Wang, B. Kang, G. Ceder, Li - Fe - P - O2 phase diagram from first principles calculations, Chem. Mater. 20 (2008) 1798–1807.
[82] C.J. Wen, R.A. Huggins, Chemical diffusion in intermediate phases in the lithium-silicon system, J. Solid State Chem. 37 (1981) 271–278.
[83] Y. Kubota, M.C.S. Escao, H. Nakanishi, H. Kasai, Crystal and electronic structure of Li15Si4, J. Appl. Phys. 102 (2007).
[84] S. Zhang, Y. Wang, G. Yang, Y. Ma, Silicon framework-based lithium silicides at high pressures, ACS Appl. Mater. Interfaces 8 (2016) 16761–16767.
[85] S.C. Jung, Y.K. Han, Ab initio molecular dynamics simulation of lithiation-induced phase-transition of crystalline silicon, Electrochim. Acta 62 (2012) 73–76.
[86] Z. Wang, M. Gu, Y. Zhou, X. Zu, J.G. Connell, J. Xiao, D. Perea, L.J. Lauhon, J. Bang, S. Zhang, C. Wang, F. Gao, Electron-rich driven electrochemical solid-state amorphization in Li-Si alloys, Nano Lett. 13 (2013) 4511–4516.
[87] P. Limthongkul, Y.I. Jang, N.J. Dudney, Y.M. Chiang, Electrochemically-driven solid-state amorphization in lithium-silicon alloys and implications for lithium storage, Acta Mater. 51 (2003) 1103–1113.
[88] J. Li, J.R. Dahn, An in situ X-ray diffraction study of the reaction of Li with crystalline Si, J. Electrochem. Soc. 154 (2007). A156.
[89] M.N. Obrovac, L.J. Krause, Reversible cycling of crystalline silicon powder, J. Electrochem. Soc. 154 (2007). A103.
[90] Z. Favors, W. Wang, H.H. Bay, A. George, M. Ozkan, C.S. Ozkan, Stable cycling of SiO2 nanotubes as high-performance anodes for lithium-ion batteries, Sci. Rep. 4 (2015) 4605.
[91] Q. Sun, B. Zhang, Z.-W. Fu, Lithium electrochemistry of SiO2 thin film electrode for lithium-ion batteries, Appl. Surf. Sci. 254 (2008) 3774–3779.
[92] H. Xia, Y.S. Meng, L. Lu, G. Ceder, Electrochemical Behavior and Li Diffusion Study of LiCo2 Thin Film Electrodes Prepared by PLD, 2007.
[93] Y. Xu, C. Stetson, K. Wood, E. Sivonxay, C. Jiang, G. Teeter, S. Pylypenko, S.D. Han, K.A. Persson, A. Burrell, A. Zakutayev, Mechanical properties and chemical reactivity of Li x SiO y thin films, ACS Appl. Mater. Interfaces 10 (2018) 38558–38564.
[94] Y. Hwa, C.M. Park, H.J. Sohn, Modified SiO as a high performance anode for Li-ion batteries, J. Power Sources 222 (2013).
[95] J.K. Lee, W.Y. Yoon, B.K. Kim, Kinetics of reaction products of silicon monoxide with controlled amount of Li-ion insertion at various current densities for Li-ion batteries, J. Electrochem. Soc. 161 (2014) A927–A933.
[96] M. Mali, J. Roos, M. Sonderegger, D. Brinkmann, P. Heitjans, 6Li and 7Li diffusion coefficients in solid lithium measured by the NMR pulsed field gradient technique, J. Phys. F Met. Phys. 18 (1988) 403–412.
[97] P. Heitjans, A. Korblein, H. Ackermann, D. Dubbers, F. Fujara, H.J. stockmann, Self-diffusion in solid lithium probed by spin-lattice relaxation of 8Li nuclei, J. Phys. F Met. Phys. 15 (1985) 41–54.
[98] A. Lodding, J.N. Mundy, A. Ott, Isotope inter- diffusion and self- diffusion in solid lithium metal, Phys. Status Solidi 38 (1970) 559–569.